Geophysical Research Letters

RESEARCH LETTER
10.1029/2023GL106853

Asymmetry of Submesoscale Instabilities in Anticyclonic and Cyclonic Eddies

Weian Shi[1], Hongyang Lin[1,2], Qiang Deng[1], and Jianyu Hu[1,2,3]

[1]State Key Laboratory of Marine Environmental Science, Department of Physical Oceanography, College of Ocean and Earth Sciences, Xiamen University, Xiamen, China, [2]Southern Marine Science and Engineering Guangdong Laboratory (Zhuhai), Zhuhai, China, [3]Center for Marine Meteorology and Climate Change, Xiamen University, Xiamen, China

Key Points:

- Distributions and evolutions of submesoscale features manifest prominent asymmetries in anticyclonic and cyclonic eddies
- Submesoscale filaments are generated in eddy-front area for both types of eddies but migrate outward (inward) for anticyclones (cyclones)
- Submesoscale asymmetries in anticyclones and cyclones are mainly determined by changes in mesoscale (background) stratification

Supporting Information:

Supporting Information may be found in the online version of this article.

Correspondence to:

H. Lin,
hylin@xmu.edu.cn

Citation:

Shi, W., Lin, H., Deng, Q., & Hu, J. (2024). Asymmetry of submesoscale instabilities in anticyclonic and cyclonic eddies. *Geophysical Research Letters*, *51*, e2023GL106853. https://doi.org/10.1029/2023GL106853

Received 16 OCT 2023
Accepted 15 JAN 2024

Abstract The upper-ocean relative vorticity has been found to be cyclonically skewed, but altimetry observations indicate that long-lifespan mesoscale eddies tend to be anticyclonic. We are thus interested in whether cyclonic or anticyclonic eddies are more unstable under similar circumstances. Here we use submesoscale-resolving simulations of idealized mesoscale eddies, incorporating theoretical analyses, to investigate asymmetries of submesoscale instabilities within the anticyclones and cyclones. It is found that submesoscale filaments initiate at regions with the largest horizontal buoyancy gradients for both anticyclones and cyclones, but these filaments subsequently rotate outward in anticyclones while inward in cyclones. Hence submesoscales are more vigorous at anticyclone peripheries and the cyclone center. Such differing distributions and evolutions of submesoscale processes are primarily caused by changes in the background stratification associated with the decaying of mesoscale eddies. The active submesoscales near the cyclone center eventually distort its core structure radically, whereas the anticyclone remains largely unaffected.

Plain Language Summary Previous studies found that flows with large anticyclonic vorticity, which is negative (positive) in the Northern (Southern) Hemisphere, tend to be suppressed from further growing due to developed instabilities. Hence large-magnitude vorticity in the real ocean is more likely to be cyclonic than anticyclonic. However, satellite observations reveal that there are more anticyclonic than cyclonic eddies that live longer in time and also propagate farther in distance. It naturally raises a question whether cyclonic or anticyclonic eddies are more unstable to instabilities. In this study, by conducting high-resolution numerical simulations of idealized mesoscale eddies, we find profound asymmetries in the spatial distributions and time evolutions of smaller-scale features (mainly submesoscale filaments) within the simulated cyclonic and anticyclonic eddies. The submesoscale filaments are first generated at regions with the largest horizontal gradients of density for both eddies, but their subsequent evolutions are different. Submesoscale filaments migrate outward within anticyclonic eddies while inward within the cyclonic eddies. Because of this evolution asymmetry, the core structure of the cyclonic eddies is significantly distorted after a certain period whereas the anticyclonic eddies keep largely unaffected. This is perhaps the reason why anticyclonic eddies tend to live longer in time.

1. Introduction

Mesoscale eddies represent a major portion of oceanic kinetic energy (Ferrari & Wunsch, 2009; Storer et al., 2022) and hence the energy budget of mesoscale eddies is of great importance in the context of global oceanic energy cascade. After decades of research, the energy source for eddies is better understood than their energy sink (e.g., Gill et al., 1974). Constrained by density stratification and Earth's rotation, geostrophic eddies tend to exhibit upscale energy transfer (Charney, 1971; Scott & Wang, 2005). Thus how mesoscale eddies dissipate becomes an intriguing and vital issue. Several mechanisms have been proposed as potential routes to eddy dissipation. For example, eddies can be damped due to viscous effect or scatter to high-wavenumber modes at boundary layers (e.g., Hughes & Wilson, 2008; Nikurashin & Ferrari, 2010; Zhai et al., 2010); mesoscale eddies can also spontaneously emit inertia-gravity waves and hence transfer their energy to unbalanced motions that are more vulnerable to dissipation (e.g., Molemaker et al., 2015). With the advancement in high-resolution ocean observations and numerical simulations, submesoscale processes have been increasingly recognized as an important mediator in the downscale transfer of eddy energy, thus bridging the gap between mesoscale and the dissipative scale (McWilliams, 2016). Moreover, submesoscale processes are characterized by much larger

vertical velocities than mesoscale processes, indicating potentially crucial roles in the vertical exchange of nutrient or heat between the surface and interior oceans (Mahadevan, 2016; Su et al., 2018).

High-resolution numerical simulations often suggest more vigorous submesoscale activities at eddy peripheries than in the eddy center (e.g., Capet et al., 2008), and some observational studies also support such a pattern (e.g., Yang et al., 2017). This paradigm, however, is recently challenged by both in situ measurements (Hu et al., 2023) and numerical modeling studies (Brannigan et al., 2017). Based on a suite of simulations with different resolutions, Brannigan et al. (2017) revealed distinct features in the growth rate and spatial distribution of submesoscale filaments within anticyclonic and cyclonic eddies; specifically, submesoscale instabilities can develop at a coarser spatial resolution with a shorter time scale in anticyclones than those in cyclones; moreover, the active submesoscale filaments seem to initiate at the peripheries of anticyclones whereas the slower-growing filaments start from the core region of cyclones. These numerical simulations demonstrate that submesoscale processes may manifest prominent asymmetries with different polarities of mesoscale eddies.

In accordance with the finding of Brannigan et al. (2017), previous investigators have also reported that anticyclonic flows are more vulnerable to submesoscale instabilities than cyclonic flows. These instabilities include (a) centrifugal or inertial instability when the absolute vorticity takes the opposite sign of planetary vorticity (e.g., Thomas et al., 2013), and (b) ageostrophic anticyclonic instability that arises in several types of shear flows (McWilliams et al., 2004). Flows with large anticyclonic vorticity are thus more easily suppressed from further growing due to these instabilities, which is often used to interpret the distribution of cyclonically skewed relative vorticity seen in the upper ocean (e.g., Lin et al., 2020; Rudnick, 2001). Whitt and Thomas (2015) also indicated that anticyclonic flows are preferentially damped when the energy of geostrophic flows is extracted by near-inertial motions. However, such an understanding seems to contradict with satellite observations of eddy activities. According to the altimeter-based global statistics of mesoscale eddies, Chelton et al. (2011) reported a slight preference for short-lived cyclonic over anticyclonic eddies; however, eddies with long lifetimes and large propagation distances are preferred to be anticyclonic (see their Figures 2–4). This is somewhat unexpected if the above argument holds (i.e., anticyclonic flows are more easily suppressed from further growing due to instabilities). We conjecture that this argument is valid subject to certain circumstances which will be examined in depth here.

In this study, we aim to characterize the asymmetric features of submesoscale processes (e.g., filaments) within cyclonic and anticyclonic eddies and explore the dynamics responsible for the asymmetries focusing on submesoscale instabilities.

2. Numerical Simulations

The high-resolution Massachusetts Institute of Technology general circulation model (MITgcm) (Marshall et al., 1997) is used here to simulate the evolutions of mesoscale eddies and their associated submesoscale features. All simulations have a squared domain that is doubly periodic with a side length of 256 km and a depth of 1,000 m. The horizontal resolution is 500 m in both zonal and meridional directions, permitting submesoscale processes in the model (e.g., Brannigan et al., 2017). There are 180 levels in the vertical and, as we mainly focus on the submesoscale processes in the upper ocean, the grid spacing increases from 1 m in the upper 100 m to 40 m near the bottom. The K-profile parameterization is used to parameterize vertical mixing (Large et al., 1994). In each experimental run, a single idealized eddy is initially prescribed by an anomalous temperature core with a Gaussian structure (i.e., warm core for anticyclones and cold core for cyclones) (Figures 1b and 1c), which then freely evolves without other forcing. The construction of the eddy follows the numerical setting of Ji et al. (2022) and Wang et al. (2022), and more details can be found in Supporting Information S1. The temperature anomaly at the eddy center is set to be ∼2°C (Figure 1a), and after ∼1 day adjustment, both the anticyclonic and cyclonic eddies have a mixed layer depth of ∼64 m at the eddy center and a radius of ∼46 km (we define the ±2 cm sea level anomaly contour as the eddy boundary because this contour is closed to positions with the maximum azimuthal velocity and contains the main structure of each idealized eddy). Although the initial temperature anomaly is the same, the anticyclone has slightly larger velocities than cyclone as the anticyclonic fronts (i.e., fronts encircling a warm core) tend to have larger angular velocities compared to cyclonic fronts (Shakespeare, 2016). Given the spatial scale of the simulated eddies, all simulations are configured on an f-plane ($f = 10^{-4}$ s^{-1}). The beta effect could affect certain aspects of the eddy evolution (e.g., westward propagation of the eddy, radiation of Rossby waves, etc.), but sensitivity runs indicate that its impact on the generation and evolution of submesoscale processes within the eddies is rather limited (figures not shown).

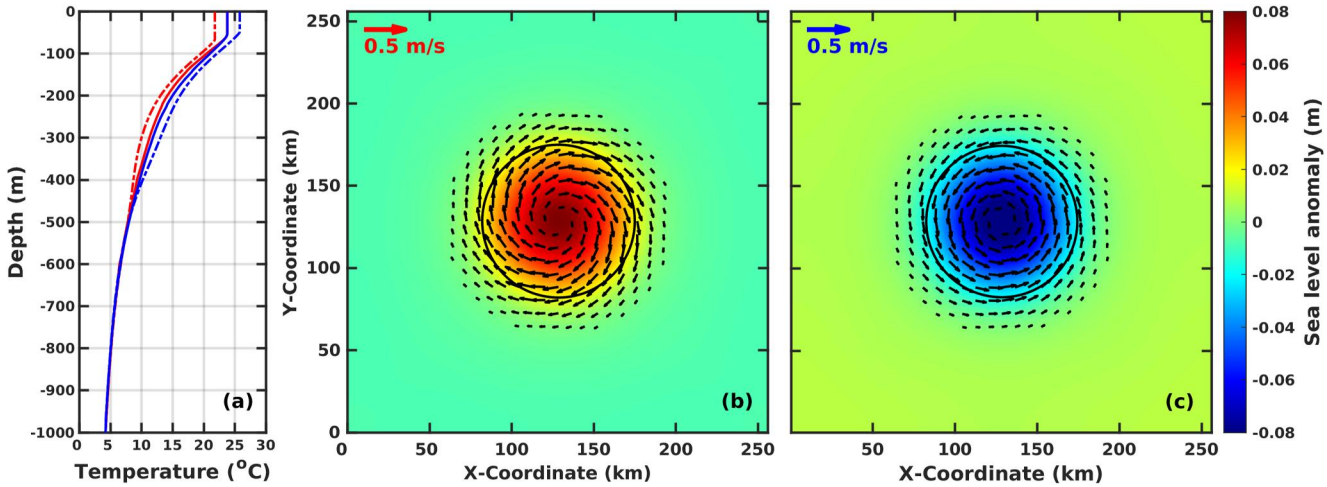

Figure 1. Initial states of two idealized eddies. (a) Vertical temperature profiles of the eddy center (solid lines) and the background (dashed lines). Blue lines for the cyclone and red lines for the anticyclone. (b–c) Sea level anomaly and sea surface velocities of the idealized anticyclone (b) and idealized cyclone (c). The black circle in (b) or (c) denotes the eddy boundary defined by the ±2 cm sea level anomaly contour.

3. Results

3.1. Simulation Results

Since the eddy is prescribed by a mesoscale temperature anomaly and then evolves without additional forcing, the entire subsequent period of interest can in fact be regarded as the eddy's decaying stage in terms of total kinetic energy of the eddy, although the associated submesoscale processes will experience stages of generation, intensification, mature and decay. For the anticyclone and cyclone presented above, submesoscale filaments start to be apparent from ~Day 8 at regions with the largest buoyancy gradient (termed as eddy-front area hereinafter and marked by the region bounded by two dashed circles in Figures 2a and 2d) for both the anticyclone and cyclone (Figures 2a and 2d). The submesoscale processes within the eddies become increasingly active during Days 14–22 and reach their strongest in about Days 23–30. Closer inspection suggests that the early-staged submesoscale filaments are located closer to the eddy core for the cyclone (Figure 2d) and their subsequent evolutions also tend to be confined within the eddy core area (Figure 2e). For the anticyclone, nevertheless, both the early-staged and subsequently developed filaments have a stronger impact on the eddy peripheries (Figures 2a and 2b). The submesoscale processes finally distort the edges of the anticyclone, with filaments leaking to the exterior region of the eddy, but the core area of the anticyclone largely remains unaffected in terms of the flow and temperature fields (Figure 2c and Figure S1a in Supporting Information S1). As for the cyclone, the eddy edge maintains the circle-like shape (Figure 2f) but the submesoscale motions have significantly distorted the core structure of the cyclone, both evidenced in the flow and temperature fields (Figure 2f and Figure S1b in Supporting Information S1). It thus becomes clear that under such model configurations submesoscale processes are more active in the central area of cyclones whereas they are more vigorous in the peripheral area of anticyclones. In fact, such asymmetrical distributions of submesoscale motions within anticyclonic and cyclonic eddies are not sensitive to moderate changes in the eddy strength (indicated by initial temperature anomalies) or eddy size (Figures S2 and S3 in Supporting Information S1).

To quantify the asymmetries of submesoscale motions in the anticyclones and cyclones, we measure the submesoscale activity level using two parameters: P_{Ro} and P_{sdg} (Wang et al., 2022):

$$P_{Ro} = \frac{n_{Ro}}{n_t} \quad (1)$$

$$P_{sdg} = \frac{n_{sdg}}{n_t} \quad (2)$$

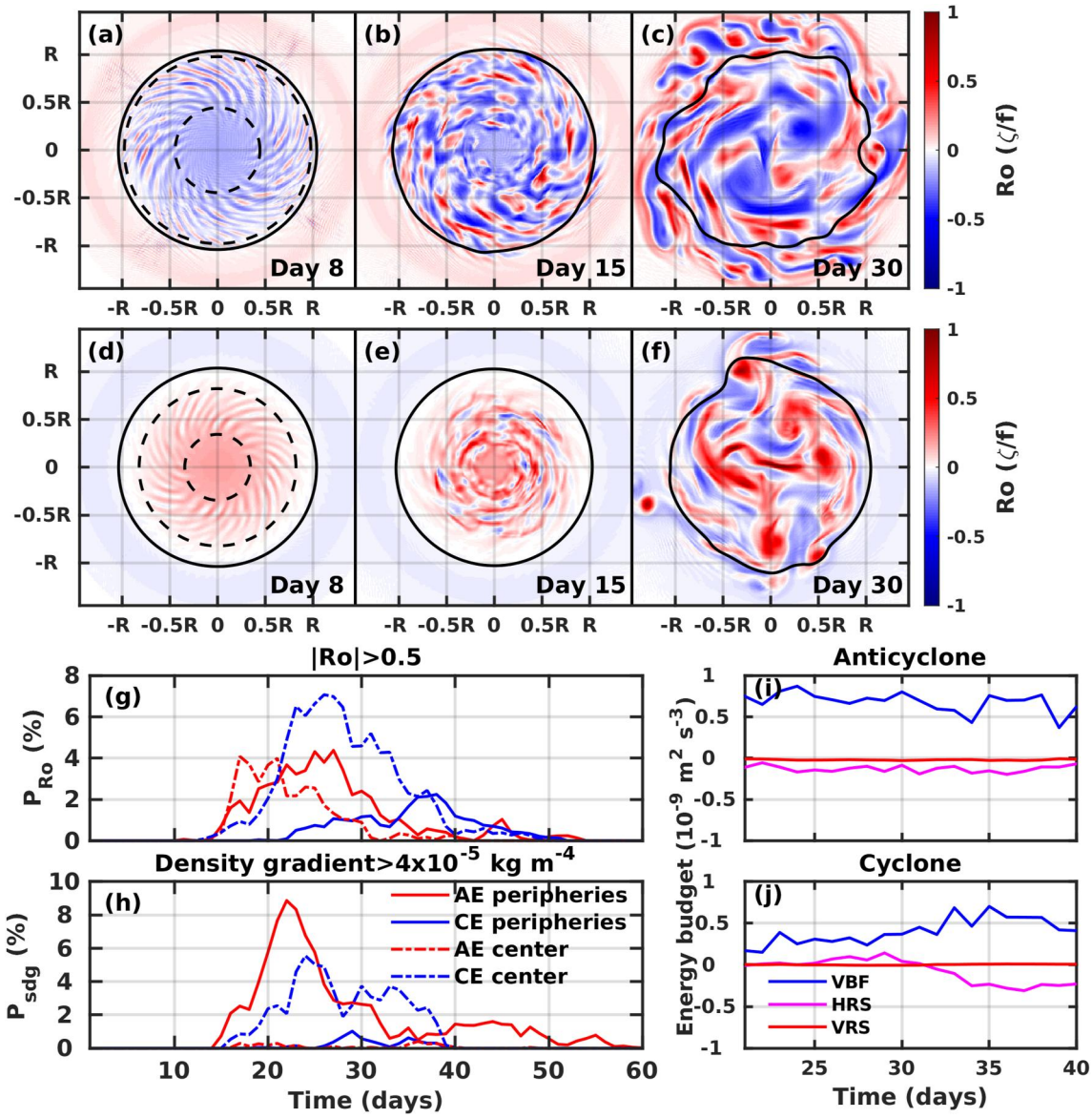

Figure 2. Spatial distributions of the surface Rossby number for anticyclone (a–c) and cyclone (d–f) at different stages (the black lines indicate the eddy edge defined by ±2 cm sea level anomaly contour, R denotes the eddy radius in initial state). The area bounded by the two dashed circles in a and d denotes the eddy-front area. (g–h) Temporal variations of (g) P_{Ro} and (h) P_{sdg} in eddy central (dashed lines) and peripheral (solid lines) areas of the anticyclone (AE, red lines) and the cyclone (CE, blue lines). (i–j) Temporal variations of the energy conversion terms (see Section 3.2 for details) averaged over the whole simulation domain of (i) the anticyclone and (j) the cyclone.

where n_{Ro} (n_{sdg}) is the number of surface grid points with Rossby number greater than 0.5 (horizontal density gradient larger than 4×10^{-5} kg m^{-4}) in a certain region and n_t is the total number of surface grid points in the corresponding region. (The Rossby number is defined here by the vertical relative vorticity scaled by local planetary vorticity.) According to Equations 1 and 2, large values of P_{Ro} and P_{sdg} indicate active submesoscale activities. We then examine the temporal variations of these two parameters over the central (0–0.7R, where R denotes eddy radius) and peripheral (0.7–1.2R) areas of the anticyclone and cyclone (Figures 2g and 2h). Note that the results are insensitive to moderate modifications to the boundaries defining the eddy central and peripheral areas.

In the first 13 days, both eddies remain relatively stable (Figures 2g and 2h), although the spatial maps of Rossby number indicate that submesoscale filaments become increasingly evident during Days 6–13 (figures not shown),

implying an enhancement in the growth rate of submesoscale processes in this period. After Day 14, the P_{Ro} starts to increase (Figure 2g), indicating increasingly important roles of submesoscale processes within the model domain. It can be seen from Figure 2g that both at eddy center and peripheries, submesoscale activities develop more rapidly in the anticyclone than in cyclone during the early stage (Days 14–21). During Days 22–29, P_{Ro} decreases in the central area while reaches a high-value plateau at eddy peripheries of anticyclone, consistent with the previous finding of an outward growing trend of submesoscale filaments for anticyclones (Figures 2a–2c). As for the cyclone, strong submesoscale activities are found in the eddy central area during Days 22–37. The peripheral area of the cyclone is barely influenced by submesoscale processes except in Day 38 when P_{Ro} reaches its largest value of ∼2%. This abrupt increase is due to the leaking of submesoscale filaments generated in the central area of cyclone. The statistics of P_{Ro} suggest that submesoscales develop in the central and peripheral areas of anticyclones during the early stage but quickly evolve to concentrate at their peripheries, while the submesoscales mainly occur in the central area of cyclones.

The statistics of P_{sdg} exhibit large values at anticyclone peripheries and the cyclone center (Figure 2h), also in good accordance with previous findings. The initial and subsequently developed filaments around the anticyclone lead to enhanced density gradients at its peripheries. By contrast, the density gradient at the center of anticyclone remains rather weak over time, confirming our previous conjecture that the core area of the anticyclone is not largely influenced by the evolution of submesoscales. As for the cyclone, since the submesoscale motions significantly deform its core area, enhanced density gradients are found at the eddy center as expected (Figure S1 in Supporting Information S1) and weak density gradients are seen at its peripheries (Figure 2h). Such distinct asymmetric distributions of submesoscales in the anticyclones and cyclones can be more clearly seen with the aid of two supplementary simulations (Figure S4 in Supporting Information S1) which are designed to permit more vigorous submesoscale motions compared to the simulations presented here (see details in Supporting Information S1).

3.2. Energetic Diagnosis

Given the asymmetric distribution of submesoscale features shown above, we are interested in the instabilities and energy transfers occurring in the anticyclones and cyclones, respectively. Following the practices of previous diagnostic analyses (e.g., Gula et al., 2016; Thomas et al., 2013), we quantify the eddy-mean energy transfers based on three quantities. The conversion from eddy potential energy to eddy kinetic energy, indicative of baroclinic instability, is calculated by the vertical buoyancy flux (VBF) $\mathrm{VBF} = \overline{w'b'}$; the conversion from mean to eddy kinetic energy, indicative of barotropic instability, can be evaluated by the horizontal shear production (HRS) $\mathrm{HRS} = \overline{-\boldsymbol{u}'v'\frac{\partial \boldsymbol{u}_b}{\partial y} - \boldsymbol{u}'u'\frac{\partial \boldsymbol{u}_b}{\partial x}}$ or the vertical shear production (VRS) $\mathrm{VRS} = \overline{-\boldsymbol{u}'w'\frac{\partial \boldsymbol{u}_b}{\partial z}}$, where $\boldsymbol{u} = (u,v,w)$ is the velocity vector in (x,y,z) directions obtained from the 500 m resolution simulation, $\boldsymbol{u_b}$ is the balanced velocity obtained from the 4 km resolution simulation at the corresponding time, b is the buoyancy. The overbar denotes a spatial average over the simulation domain, and the prime denotes perturbations defined by the difference between the simulation at 500 m resolution and the simulation at 4 km resolution (Brannigan, 2016). More specifically, when negative Ertel potential vorticity is primarily contributed by positive HRS, centrifugal or inertial instability develops, and if it is mainly contributed by positive VRS, symmetric instability develops (Thomas et al., 2013). The three conversion terms are spatially averaged over the simulation domain and their temporal variations are examined (Figures 2i and 2j).

For the simulations presented here, large Rossby number (>0.5) only appears in the upper 74 m of anticyclone but the upper 65 m of cyclone, indicating that submesoscale processes are mainly confined within the mixed layer. Hence we perform the energetic diagnoses for the upper 100 m of the whole simulation domain for the simulation period Days 21–40 when the submesoscale processes are vigorous. It is shown that VBF is positive in both the anticyclone and cyclone (Figures 2i and 2j), implying that baroclinic instability arises in both eddies when submesoscale processes are active. In both the anticyclone and cyclone, the magnitude of VRS is much smaller than that of HRS. The near-zero VRS suggests that symmetric instability does not occur in either anticyclone or cyclone. Brannigan (2016) found evidence of symmetric instability occurring in a high-resolution simulation of an anticyclone, but unlike our simulations, simulations of Brannigan (2016) include zonal wind forcing which might be effective in triggering symmetric instability. It should be noted that in cyclone HRS is positive during Days 22–31 and turns to negative after that but in anticyclone it is always negative. The positive values of both VBF and HRS (in the time that submesoscales reaches their peak) indicate that the cyclones are unstable to a

mixture of barotropic and baroclinic instabilities which transfer the mechanical energy of the cyclones toward smaller scales. By contrast, the downscale energy transfer within the anticyclones is mainly via baroclinic instability while the horizontal shears tend to contribute upscale energy transfer (Figure 2i). The differing instabilities developed in the anticyclones and cyclones are consistent with findings of previous studies (Brannigan et al., 2017; de Marez et al., 2020; Wang et al., 2022).

4. Dynamical Interpretations

4.1. Theories

Following Bachman and Taylor (2014), we start from the primitive equations in a cylindrical coordinate system $\boldsymbol{x} = (r,\theta,z)$ on an f-plane (with r,θ,z being radial, azimuthal and vertical directions), and combine the perturbation equations into a single equation in terms of u' (i.e., the perturbation flow in r direction; the prime would be neglected hereinafter):

$$\left(\frac{\partial}{\partial t}\right)^2\frac{\partial^2 u}{\partial z^2}+\beta\left(\frac{\partial}{\partial t}\right)^2\left(\frac{\partial^2 u}{\partial r^2}+\frac{1}{r_0}\frac{\partial u}{\partial r}\right)-M^2\frac{\partial^2 u}{\partial r\partial z}+N^2\left(\frac{\partial^2 u}{\partial r^2}+\frac{1}{r_0}\frac{\partial u}{\partial r}\right)-M^2\frac{\partial}{\partial z}\left(\frac{\partial u}{\partial r}+\frac{u}{r_0}\right)+A(Z+f)\frac{\partial^2 u}{\partial z^2}=0 \tag{3}$$

where β is the hydrostatic parameter ($\beta = 0$ for hydrostatic and $\beta = 1$ for non-hydrostatic), M^2 is the radial buoyancy gradient ($\frac{\partial b}{\partial r}$), N^2 is the squared buoyancy frequency ($\frac{\partial b}{\partial z}$), $A = 2\Omega + f$ with Ω being angular velocity at a reference radius r_0, f is Coriolis parameter, Z is relative vorticity which equals to 2Ω in the cylindrical coordinate. The detailed derivation of Equation 3 is provided in Supporting Information S1. The viscous term has been neglected in Equation 3, but it is noted that the vertical viscous term acts against the growth of submesoscales both in cyclonic and anticyclonic eddies (see Supporting Information S1), which will not be examined in this work. We seek solutions in the form of $u = \hat{u}e^{ikr+imz+\sigma t}$ with k and m being radial and vertical wavenumbers, respectively. When $\beta = 0$, the expression of the submesoscale growth rate σ has the same form with that in Brannigan et al. (2017). When $\beta = 1$ and terms with $\frac{1}{r_0}$ are neglected, the expression of σ would be the same with that in Buckingham et al. (2021). Now we set $\beta = 1$ and substitute $u = \hat{u}e^{ikr+imz+\sigma t}$ into Equation 3 and we can get the following two equations:

$$\left(m^2+k^2\right)\sigma^2 = 2kmM^2 - k^2N^2 - A(Z+f)\,m^2 \tag{4}$$

$$\frac{1}{r_0}k\sigma^2 i = \frac{1}{r_0}mM^2 i - \frac{1}{r_0}kN^2 i \tag{5}$$

Both Equations 4 and 5 suggest that either strong lateral buoyancy gradient (M^2) or weak stratification (N^2) is conducive to the development of submesoscale instabilities. Equation 4 can be rearranged as:

$$\sigma^2 = \frac{-\left(\frac{k}{m}\right)^2N^2 + 2\,\frac{k}{m}M^2 - A(Z+f)}{1+\left(\frac{k}{m}\right)^2} \tag{6}$$

Equation 6 indicates a necessary condition for submesoscale instabilities to arise (e.g., Buckingham et al., 2021; Hoskins, 1974), namely the discriminant of the numerator must be positive to allow for $\sigma^2 > 0$:

$$4M^4 - 4N^2A(Z+f) > 0 \tag{7}$$

We further substitute $Z = 2\Omega$ and rearrange Equation 7 as:

$$\frac{N^2}{M^4} < \frac{1}{A(Z+f)} = \frac{1}{(Z+f)^2} \tag{8}$$

Assuming thermal wind balance, we have $M^2 = A\frac{\partial V}{\partial z}$; similar to Thomas et al. (2013), we define the balanced Richardson number as squared buoyancy frequency divided by the geostrophic shear (or the horizontal buoyancy gradient), and then Equation 8 becomes:

$$Ri_B = \frac{N^2}{\left(\frac{\partial V}{\partial z}\right)^2} < \frac{A}{(Z+f)} = 1 \tag{9}$$

More vigorous submesoscales are expected to be accompanied by lower Ri_B. Equation 8 indicates that with the same buoyancy frequency and lateral buoyancy gradient, fronts are more unstable when their relative vorticity Z takes the opposite sign of the Coriolis parameter f (i.e., anticyclonic fronts).

4.2. Impact of the Mesoscale Evolution on Submesoscale

We now investigate the evolution of submesoscale processes inside mesoscale eddies. Specifically, we aim to answer two main questions: (a) where do submesoscale processes initiate? (b) Where does the most unstable mode for submesoscales exist (i.e., where the growth rate σ is largest)? As mentioned above, the first question can be answered by identifying regions with low values of Ri_B, that is, regions with weak stratification or strong horizontal buoyancy gradients. The second question can be explored by inspecting Equation 6, which indicates that σ depends on N^2, M^2 and $A(Z+f)$ of which the typical magnitudes are on the order of 10^{-4}, 10^{-7}, and 10^{-8} s^{-2}, respectively. The daily changes of N^2, M^2 and $A(Z+f)$ in our simulations are on the magnitude of 10^{-6}, 10^{-8}, and 10^{-8} s^{-2}, respectively. Hence the most unstable mode of submesoscale growth rate σ is determined primarily by the stratification N^2 within eddies.

We first examine the lateral buoyancy gradients in both eddies. Although the initial temperature anomaly is the same, the anticyclone would have larger vertical velocity shears than the cyclone according to the gradient wind balance. The magnitude of Ri_B is thus lower in the anticyclone resulting in a larger range of submesoscale filaments (see Figures 3a, 3b, 2a, and 2d). This implies that the anticyclone is expected to be more favorable to submesoscale instabilities. Given the symmetric feature of eddy structures, it can be assumed that both horizontal velocity and its vertical shear is near 0 at eddy center, which means that Ri_B is very large and Equation 9 is probably not satisfied. We thus infer that the central area of eddies is free of submesoscale instabilities unless it is influenced by submesoscale filaments leaking from nearby. Therefore, we find that submesoscale processes initially occur at the eddy-front area where horizontal buoyancy gradient is most prominent, and this answers the first question.

Next we examine the stratification changes in both eddies trying to identify where the most unstable mode exists. As the eddy evolution is a mesoscale process, we perform new simulations of the same idealized anticyclone and cyclone but in a coarser 4-km horizontal resolution, of which submesoscale processes are not resolved. Here we denote mesoscale stratification from the 4-km resolution simulation as N_m^2 and submesoscale stratification from the 500-m resolution simulation as N_{sm}^2. The temporal change of mesoscale stratification (ΔN_m^2) is defined as the difference of N_m^2 between two temporal stages, whereas the temporal change of submesoscale stratification (ΔN_{sm}^2) is defined as the difference of $\left(N_{sm}^2 - N_m^2\right)$ between two temporal stages. Note that submesoscale processes are already vigorous after Day 14 (Figures 2b, 2e, 2g, and 2h), while we are interested in the period when the submesoscale growth rate is highest, so we focus on stratification changes during Days 6–13 when submesoscale filaments are becoming increasingly active.

Since the mesoscale eddies are decaying during the entire simulation period, the elevated isopycnals at anticyclone peripheries and the cyclone center would fall down, leading to the vertical stretching of isopycnals (i.e., decreasing stratification). This stratification change due to mesoscale evolution is confirmed by the negative ΔN_m^2 at anticyclone peripheries and the cyclone center, either based on a 7-day interval (Day 13 minus Day 6; Figures 3g and 3h) or 1-day interval (Day 9 minus Day 8; Figures 3i and 3j). These mesoscale (background) stratification changes provide conducive conditions for the generation and evolution of submesoscales at the corresponding areas of anticyclone and cyclone (Figures 2, 3a and 3b). The developed submesoscale activities would then restratify the upper ocean, which is also confirmed by the positive ΔN_{sm}^2 in the above areas (Figures 3c–3f). As mentioned above, enhanced submesoscale growth rate is primarily contributed by decreased

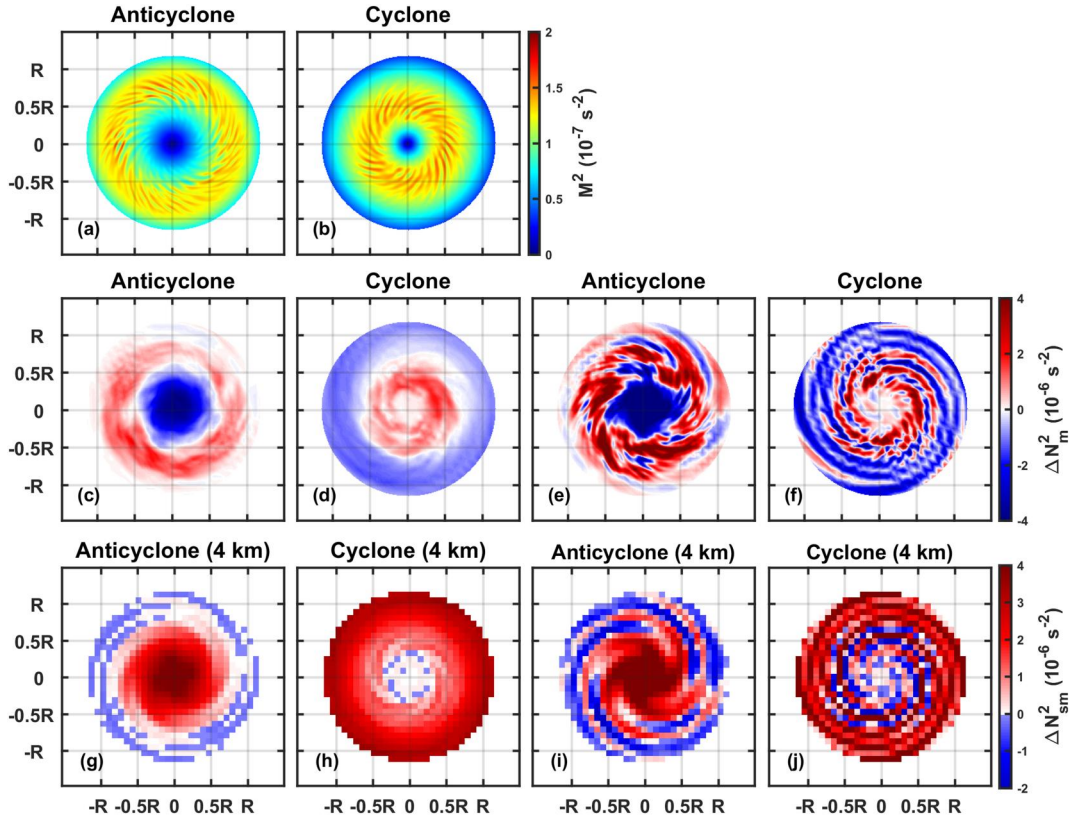

Figure 3. (a–b) Distributions of lateral buoyancy gradient (M^2) in Day 8 of anticyclone (a) and cyclone (b) from the submesoscale-resolving simulations (500-m horizontal resolution). (c–d) Changes of submesoscale buoyancy frequency (ΔN^2_{sm}) at the mid-depth of mixed layer (30–40 m) of anticyclone (c) and cyclone (d) between Day 6 and Day 13. (e–f) Similar to (c–d) but for the changes between Day 8 and Day 9. (g–j) Similar to (c–f) but for mesoscale simulations with a 4-km horizontal resolution (ΔN^2_m).

stratification. We can answer the second question by summarizing the above findings: (a) mesoscale eddy evolution causes a decrease in the background stratification at different areas for anticyclones and cyclones, (b) decreased mesoscale stratification is conducive to the rapid development of the most unstable mode for submesoscales, and (c) the developed submesoscale processes induce restratification which in turn increases stratification at submesoscale. Because of these rationales, we observe decreased mesoscale stratification but increased submesoscale stratification at anticyclone peripheries and the cyclone center.

5. Summary and Discussion

Based on submesoscale-resolving simulations of idealized mesoscale eddies, we observe profound asymmetries of submesoscale features in the anticyclones and cyclones. Submesoscale filaments start to develop at regions with the largest horizontal buoyancy gradients M^2 (i.e., eddy-front area). Even though both eddies are prescribed with the same initial M^2, the anticyclone has a larger vertical shear of horizontal velocity according to the gradient wind balance, and is thus more favorable for the growth of submesoscale processes. With the decaying of mesoscale eddies, the background stratification N^2 decreases in the central area of cyclones and peripheral area of anticyclones, which is conducive for the growth of the most unstable mode of submesoscale instabilities. Hence submesoscale activities are more active in the corresponding areas of the anticyclones and cyclones. The developed submesoscales in turn increase N^2 due to the restratification process. Moreover, as the most unstable mode occurs at anticyclone peripheral and cyclone central areas, the submesoscale filaments initially developed at eddy-front area subsequently migrate to anticyclone peripheries and cyclone center under the mesoscale advection effect. In other words, the filaments rotate outward in the anticyclones while inward in the cyclones, exhibiting prominent asymmetric evolutionary characteristics for the submesoscale processes.

It is worthwhile to compare our findings and interpretations on the submesoscale asymmetries in mesoscale eddies with previous studies. Since the work of Hoskins (1974), numerous studies have been using Ertel potential vorticity as an important quantity to diagnose instabilities, such as symmetric, inertial or gravitational instabilities (e.g., Thomas et al., 2013). These studies regard ocean flows with large anticyclonic vorticity as more vulnerable to be unstable. Adopting ideas from the atmospheric science, recent studies take into account the impact of curvature on the submesoscale instabilities (e.g., Brannigan et al., 2017; Buckingham et al., 2021; Shakespeare, 2016). Combining these works with analyses shown in the present study, we find that *with the same lateral buoyancy gradient M^2 and stratification N^2*, as $A_{CE}(Z_{CE}+f) > A_{AE}(Z_{AE}+f)$, our Equation 8 indicates that *anticyclones are more vulnerable to submesoscale instabilities*. This is consistent with most previous studies (e.g., Brannigan et al., 2017; Shakespeare, 2016). Equation 9 indicates a necessary condition for submesoscale instabilities in curved fronts: $Ri_B = \frac{N^2}{(\partial V/\partial z)^2} < \frac{A}{Z+f} = 1$, which means that *with the same vertical shear and stratification N^2, the vulnerability to submesoscale instabilities is the same for anticyclonic front and cyclonic front*. If the curvature effect is neglected, the condition would be reduced to the condition provided by Hoskins (1974): $Ri_B = \frac{N^2}{(\partial V/\partial z)^2} < \frac{f}{Z+f}$.

As the initially developed submesoscale filaments in the cyclones subsequently rotate inward, this rotationally converging evolutions eventually distort the cyclones' core structure radically (including the thermal structure and flow field). Meanwhile, simulations presented here and those of Brannigan et al. (2017) both show that the HRS is only positive when submesoscale processes are very vigorous in the cyclones (transferring the eddy's kinetic energy to smaller scales). These two effects finally lead to the breakup of mesoscale cyclonic eddies. Conversely, the diverging evolutions of submesoscale filaments in the anticyclones do not significantly change the anticyclones' core structure and also the HRS always fuels to them. We regard this as the reason why long-lifespan eddies tend to be anticyclonic over cyclonic in the real ocean as observed by satellite altimetry. An example given in Supporting Information S1 (Figure S5) can be viewed as an evidence for the above interpretation. Nevertheless, the reason why HRS takes the opposite sign for the anticyclones and cyclones when submesoscales reach their peaks needs to be explored. Besides, as the simulations are run without additional forcing or a background flow, we are actually examining the decaying stage of isolated eddies. In the real ocean, the external forcing and background flow may also have a strong impact on the generation and evolution of submesoscale instabilities in mesoscale eddies by changing the vertical shear and stratification, which deserve further exploration in the next step.

Data Availability Statement

The data used to generate figures in this study are available in Shi (2023). The MITgcm model code is available online (Campin et al., 2023).

Acknowledgments
This work was supported by the National Natural Science Foundation of China (42076013, 91958203, 92258301). We thank the Editor and two anonymous reviewers for providing constructive comments and suggestions that helped improve an early version of the manuscript.

References

Bachman, S. D., & Taylor, J. R. (2014). Modelling of partially-resolved oceanic symmetric instability. *Ocean Modelling*, *82*, 15–27. https://doi.org/10.1016/j.ocemod.2014.07.006

Brannigan, L. (2016). Intense submesoscale upwelling in anticyclonic eddies. *Geophysical Research Letters*, *43*(7), 3360–3369. https://doi.org/10.1002/2016gl067926

Brannigan, L., Marshall, D. P., Naveira Garabato, A. C., George Nurser, A. J., & Kaiser, J. (2017). Submesoscale instabilities in mesoscale eddies. *Journal of Physical Oceanography*, *47*(12), 3061–3085. https://doi.org/10.1175/jpo-d-16-0178.1

Buckingham, C. E., Gula, J., & Carton, X. (2021). The role of curvature in modifying frontal instabilities. part I: Review of theory and presentation of a nondimensional instability criterion. *Journal of Physical Oceanography*, *51*(2), 299–315. https://doi.org/10.1175/jpo-d-19-0265.1

Campin, J.-M., Heimbach, P., Losch, M., Forget, G., Hill, E., Adcroft, A., et al. (2023). MITgcm/MITgcm: ckeckpoint68r [Software]. Zenodo. https://doi.org/10.5281/zenodo.8208482

Capet, X., McWilliams, J. C., Molemaker, M. J., & Shchepetkin, A. F. (2008). Mesoscale to submesoscale transition in the California Current System. Part II: Frontal processes. *Journal of Physical Oceanography*, *38*(1), 44–64. https://doi.org/10.1175/2007jpo3672.1

Charney, J. G. (1971). Geostrophic turbulence. *Journal of the Atmospheric Sciences*, *28*(6), 1087–1095. https://doi.org/10.1175/1520-0469(1971)028<1087:gt>2.0.co;2

Chelton, D. B., Schlax, M. G., & Samelson, R. M. (2011). Global observations of nonlinear mesoscale eddies. *Progress in Oceanography*, *91*(2), 167–216. https://doi.org/10.1016/j.pocean.2011.01.002

de Marez, C., Meunier, T., Morvan, M., L'hégaret, P., & Carton, X. (2020). Study of the stability of a large realistic cyclonic eddy. *Ocean Modelling*, *146*, 101540. https://doi.org/10.1016/j.ocemod.2019.101540

Ferrari, R., & Wunsch, C. (2009). Ocean circulation kinetic energy: Reservoirs, sources and sinks. *Annual Review of Fluid Mechanics*, *41*(1), 253–282. https://doi.org/10.1146/annurev.fluid.40.111406.102139

Gill, A. E., Green, J. S. A., & Simmons, A. J. (1974). Energy partition in the large-scale ocean circulation and the production of mid-ocean eddies. In *Deep sea research and oceanographic abstracts* (Vol. 21(7), pp. 499–528). https://doi.org/10.1016/0011-7471(74)90010-2

Gula, J., Molemaker, M. J., & McWilliams, J. C. (2016). Topographic generation of submesoscale centrifugal instability and energy dissipation. *Nature Communications*, *7*(1), 12811. https://doi.org/10.1038/ncomms12811

Hoskins, B. J. (1974). The role of potential vorticity in symmetric stability and instability. *Quarterly Journal of the Royal Meteorological Society*, *100*(425), 480–482. https://doi.org/10.1002/qj.49710042520

Hu, Z., Lin, H., Liu, Z., Cao, Z., Zhang, F., Jiang, Z., et al. (2023). Observations of a filamentous intrusion and vigorous submesoscale turbulence within a cyclonic mesoscale eddy. *Journal of Physical Oceanography*, *53*(6), 1615–1627. https://doi.org/10.1175/JPO-D-22-0189.1

Hughes, C. W., & Wilson, C. (2008). Wind work on the geostrophic ocean circulation: An observational study of the effect of small scales in the wind stress. *Journal of Geophysical Research*, *113*(C2), C02016. https://doi.org/10.1029/2007JC004371

Ji, J., Dong, C., Liu, X., Liu, T., Yu, Y., Sian, K. T. L. K., et al. (2022). Influence of oceanic mesoscale eddy on the atmospheric boundary layer based on an idealized model. *Deep Sea Research Part II: Topical Studies in Oceanography*, *202*, 105146. https://doi.org/10.1016/j.dsr2.2022.105146

Large, W. G., McWilliams, J. C., & Doney, S. C. (1994). Oceanic vertical mixing—A review and a model with a nonlocal boundary-layer parameterization. *Review of Geophysics*, *32*(4), 363–403. https://doi.org/10.1029/94rg01872

Lin, H., Liu, Z., Hu, J., Menemenlis, D., & Huang, Y. (2020). Characterizing meso- to submesoscale features in the South China Sea. *Progress in Oceanography*, *188*, 102420. https://doi.org/10.1016/j.pocean.2020.102420

Mahadevan, A. (2016). The impact of submesoscale physics on primary productivity of plankton. *Annual Review of Marine Science*, *8*(1), 161–184. https://doi.org/10.1146/annurev-marine-010814-015912

Marshall, J., Adcroft, A., Hill, C., Perelman, L., & Heisey, C. (1997). A finite-volume, incompressible Navier Stokes model for studies of the ocean on parallel computers. *Journal of Geophysical Research*, *102*(C3), 5753–5766. https://doi.org/10.1029/96jc02775

McWilliams, J. C. (2016). Submesoscale currents in the ocean. *Proceedings of the Royal Society A: Mathematical, Physical and Engineering Sciences*, *472*(2189), 20160117. https://doi.org/10.1098/rspa.2016.0117

McWilliams, J. C., Molemaker, M. J., & Yavneh, I. (2004). Ageostrophic, anticyclonic instability of a geostrophic, barotropic boundary current. *Physics of Fluids*, *16*(10), 3720–3725. https://doi.org/10.1063/1.1785132

Molemaker, M. J., McWilliams, J. C., & Dewar, W. K. (2015). Submesoscale instability and generation of mesoscale anticyclones near a separation of the California Undercurrent. *Journal of Physical Oceanography*, *45*(3), 613–629. https://doi.org/10.1175/jpo-d-13-0225.1

Nikurashin, M., & Ferrari, R. (2010). Radiation and dissipation of internal waves generated by geostrophic motions impinging on small-scale topography: Theory. *Journal of Physical Oceanography*, *40*(5), 1055–1074. https://doi.org/10.1175/2009jpo4199.1

Rudnick, D. L. (2001). On the skewness of vorticity in the upper ocean. *Geophysical Research Letters*, *28*(10), 2045–2048. https://doi.org/10.1029/2000gl012265

Scott, R. B., & Wang, F. (2005). Direct evidence of an oceanic inverse kinetic energy cascade from satellite altimetry. *Journal of Physical Oceanography*, *35*(9), 1650–1666. https://doi.org/10.1175/jpo2771.1

Shakespeare, C. J. (2016). Curved density fronts: Cyclogeostrophic adjustment and frontogenesis. *Journal of Physical Oceanography*, *46*(10), 3193–3207. https://doi.org/10.1175/jpo-d-16-0137.1

Shi, W. (2023). Asymmetry of submesoscale instabilities in anticyclonic and cyclonic eddies [Dataset]. OSF. https://osf.io/z6kcn/

Storer, B. A., Buzzicotti, M., Khatri, H., Griffies, S. M., & Aluie, H. (2022). Global energy spectrum of the general oceanic circulation. *Nature Communications*, *13*(1), 5314. https://doi.org/10.1038/s41467-022-33031-3

Su, Z., Wang, J., Klein, P., Thompson, A. F., & Menemenlis, D. (2018). Ocean submesoscales as a key component of the global heat budget. *Nature Communications*, *9*(1), 775. https://doi.org/10.1038/s41467-018-02983-w

Thomas, L. N., Taylor, J. R., Ferrari, R., & Joyce, T. M. (2013). Symmetric instability in the Gulf Stream. *Deep Sea Research Part II: Topical Studies in Oceanography*, *91*, 96–110. https://doi.org/10.1016/j.dsr2.2013.02.025

Wang, Y., Dong, J., Ji, C., & Dong, C. (2022). Dependence of submesoscale simulation on turbulence closure schemes in the Regional Ocean Modelling Modeling System (ROMS). *Ocean Modelling*, *180*, 102120. https://doi.org/10.1016/j.ocemod.2022.102120

Whitt, D. B., & Thomas, L. N. (2015). Resonant generation and energetics of wind-forced near-inertial motions in a geostrophic flow. *Journal of Physical Oceanography*, *45*(1), 181–208. https://doi.org/10.1175/jpo-d-14-0168.1

Yang, Q., Zhao, W., Liang, X., Dong, J., & Tian, J. (2017). Elevated mixing in the periphery of mesoscale eddies in the South China Sea. *Journal of Physical Oceanography*, *47*(4), 895–907. https://doi.org/10.1175/jpo-d-16-0256.1

Zhai, X., Johnson, H., & Marshall, D. (2010). Significant sink of ocean-eddy energy near western boundaries. *Nature Geoscience*, *3*(9), 608–612. https://doi.org/10.1038/ngeo943